

Directed rescue strategy for enhanced implant osteointegration in aged rats

Received: 13 October 2024

Accepted: 9 October 2025

Published online: 24 November 2025

 Check for updates

Xuan Li^{1,2,6}, Xiao Jiang^{1,6}, Ye He³, Hongwei Xiong¹, Qian Huang¹, Kun Xu¹, Xin-Xin Luo¹, Kai Li⁴, Bailong Tao⁴, Kangkang Zha⁵, Jing Wu¹, Peng Liu¹ & Kaiyong Cai¹ ✉

The elimination of senescent cells can enhance the osteointegration of implants in elderly patients. However, achieving specific clearance of senescent cells without adversely affecting the function of normal cells remains challenging. Here we show an implant surface modification technique to achieve specific clearance of locally senescent cells by modulating their metabolism. Our method involve modifying implants with BPTES, a glutaminase 1 (GLS1) inhibitor, through π - π stacking with dopamine. This modification effectively induces intracellular acidosis in senescent mesenchymal stem cells (MSCs) through suppression of glutaminolysis. Simultaneously, poly(γ -glutamate) (PGA), modified by a layer-by-layer method, serve as a high-density carbon source coating, continuously supporting glutamine metabolism in MSCs without ammonia production. Our results show that modified implants significantly reduce the senescence level around implants and promote osteointegration in aged rats. These findings provide promising insights into the design and application of orthopedic implants for elderly patients.

The accumulation of senescent cells is a primary driver of tissue deterioration and the onset of age-related degenerative diseases¹⁻³. The elimination of senescent cells has been shown to restore the function of various tissues, including the skeleton⁴⁻⁷. However, most senolytics achieve this by broadly inhibiting anti-apoptotic pathways, which can adversely affect normal cell functions and lead to significant side effects^{8,9}. In the scenario of orthopedic disease treatment, such adverse effects on normal cells may result in implant loosening or even failure. Therefore, there is an urgent need for strategies that specifically target senescent cells while preserving the function of normal cells to improve the osteointegration of implants in elderly patients.

Senescent cells exhibit increased expression of anti-apoptotic factors, such as BCL2 family members, which helps them resist apoptosis induced by the damage of various macromolecules, including DNA and proteins^{10,11}. This characteristic suggests that targeting these

anti-apoptotic factors could be a viable strategy for treating age-related degenerative diseases^{12,13}. However, the use of most senolytics that target these factors has been limited by severe side effects, including anemia, thrombocytopenia, and cytotoxicity¹⁴⁻¹⁶. Although high levels of anti-apoptotic factors enable the survival of senescent cells, the persistence of macromolecular damage continues to adversely affect cell behaviors. Specifically, cytosolic DNA fragments (including chromatin fragments and mitochondrial DNA) and misfolded proteins contribute to the activation of senescence-associated secretory phenotype (SASP)¹⁷⁻¹⁹. Furthermore, these damaged macromolecules exacerbate lysosome stress and lead to lysosomal membrane damage²⁰⁻²². This damage not only causes the accumulation of defective mitochondria^{23,24}, but also disrupts intracellular pH balance²⁵. These changes collectively alter the metabolic profile of senescent cells (e.g., SASP factors secretion, increased oxidative stress, enhanced

¹Key Laboratory of Biorheological Science and Technology, Ministry of Education College of Bioengineering, Chongqing University, Chongqing, PR China.

²Life Sciences Institute, School of Life Sciences and Medical Engineering, Guangxi Medical University, Nanning, PR China. ³Thomas Lord Department of Mechanical Engineering and Materials Science, Duke University, Durham, NC, USA. ⁴Laboratory Research Center, The First Affiliated Hospital of Chongqing Medical University, Chongqing, PR China. ⁵Department of Orthopedics, Union Hospital, Tongji Medical College, Huazhong University of Science and Technology, Wuhan, PR China. ⁶These authors contributed equally: Xuan Li, Xiao Jiang. ✉ e-mail: kaiyong_cai@cqu.edu.cn

glutamine metabolism), presenting an opportunity to induce apoptosis specifically in senescent cells through targeted metabolic intervention with minimal side effects^{7,25,26}.

Interestingly, metabolic rewiring also influences the fate of MSCs. The stemness maintenance and differentiation of MSCs is highly dependent on glycolysis²⁷, and increased glucose uptake by MSCs facilitates implant osteointegration²⁸. Enhanced fatty acid oxidation (FAO) and glutamine metabolism further support bone formation, while their inhibition impairs MSC osteogenic differentiation^{29,30}. Unlike senescent cells, inhibition of glutamine metabolism does not compromise MSC survival, due to differing glutamine metabolism requirements. Senescent cells rely on glutaminolysis for ammonia production to stabilize intracellular pH²⁵, whereas MSCs use glutamine metabolism for carbon source essential for osteogenic differentiation^{31,32}. This differential dependence on glutamine metabolism offers a promising approach for selectively inducing apoptosis in senescent cells while promoting osteogenic differentiation of MSCs through metabolic intervention, thereby enhancing implant osteointegration in elderly patients.

Based on this, we develop a straightforward method for implant surface modification to accelerate osteointegration in aged rats through a directed rescue strategy (Fig. 1). Briefly, BPTES is modified onto the surface of implants in a single step by co-incubation with dopamine, calcium ions, and amino-modified implants to broadly inhibit glutaminolysis. Subsequently, PGA and chitosan undergo spontaneous self-assembly on the implant surface through charge interaction to enhance glutamate availability at implant-host interfaces. We hypothesize that the modified implants will specifically induce apoptosis in senescent MSCs by restricting glutaminolysis while rescuing glutamine metabolism in non-senescent MSCs by supplementing glutamate without ammonia production. Additionally, the topological structure of the implant surface and enhanced glutamine metabolism are expected to synergistically promote MSC osteogenic differentiation, thereby accelerating implant osteointegration in aged rats.

Results

GLS1 maintained the survival of senescent MSCs

The inhibition of GLS1-dependent glutaminolysis has been identified as a potential strategy for eliminating senescent cells and restoring functions of multiple organs²⁵. To investigate the critical role of GLS1 in the survival of senescent MSCs, we established two different senescence models of MSCs (Supplementary Fig. 1A). The success of senescence model construction was confirmed through SA- β -gal staining, immunofluorescence staining (p16 and p21 were selected as the markers of senescence), and flow cytometry analysis (Supplementary Fig. 1B–D). Western blot results further showed that elevated expression of kidney-type glutaminase (KGA, one of the splicing variants of GLS1) in both replicative senescent MSCs (r-Sen) and induced-senescent MSCs (i-Sen), compared to non-senescent MSCs (non-Sen) (Supplementary Fig. 2A), aligns with a previous study²⁵.

To further validate the significance of GLS1 in the survival of senescent MSCs, BPTES, an inhibitor of GLS1, was used. As shown in Supplementary Fig. 2B, treatment with BPTES for 24 h led to a marked reduction in the viability of both i-Sen and r-Sen MSCs, with cell viability dropping below 50% of the initial levels and continuing to decline over time. Flow cytometry confirmed that BPTES significantly induced apoptosis in i-Sen and r-Sen, while non-Sen remained unaffected (Supplementary Fig. 2C). These results underscore the essential role of GLS1 in the survival of senescent MSCs. For subsequent experiments, i-Sen was selected as the senescence model of MSCs.

The apoptosis of senescent cells induced by BPTES was associated with intracellular acidosis and its mediated activation of the BCL2 and adenovirus E1B 19-kDa-interacting protein 3 (BNIP3) and mitochondrial permeability transition pore (mPTP) axis²⁵. To further investigate

the molecular mechanism of BPTES-induced apoptosis in senescent MSCs, a pan-caspase inhibitor (Z-VAD-FMK) was used to verify whether BPTES induces apoptosis in senescent MSCs via a caspase-dependent pathway (Supplementary Fig. 3A). The results showed that cyclosporine A (CsA, an mPTP inhibitor), but not Z-VAD-FMK, could effectively inhibit apoptosis, suggesting that BPTES-induced apoptosis in senescent MSCs occurs through a caspase-independent mechanism. Western blot analysis confirmed that senescent MSCs treated with BPTES still showed a tight mitochondrial association with BNIP3 after alkaline treatment (Supplementary Fig. 3B), consistent with the characteristics of acidosis-induced apoptotic pathways^{25,33,34}. Furthermore, significantly reduced intracellular pH levels and significantly opened mPTP in the BPTES and BPTES&PGA groups compared to the Control and PGA groups further validated the occurrence of intracellular acidosis and its mediated apoptosis (Supplementary Fig. 3C, D). Notably, the presence of PGA did not affect the pro-apoptotic effect of BPTES, which ensures the possibility of its use as a rescue donor for glutamine metabolism in non-senescent MSCs. Interestingly, BPTES could also lead to a significant reduction in the viability of senescent endothelial cells (ECs) and senescent osteoblasts (Supplementary Fig. 4), suggesting its potential broad-spectrum senolytic effects within bone tissue. This observation aligns with its demonstrated broad-spectrum senolytic activity across various tissues²⁵.

PGA rescued glutamine metabolism of non-senescent MSCs

The inhibition of glutamine metabolism limits the production of α -ketoglutarate (α -KG), thereby severely impairing the proliferation and osteogenic differentiation of non-senescent MSCs³². To assess the potential adverse effects of BPTES on non-senescent MSCs and evaluate the therapeutic capacity of PGA in restoring glutamine metabolic homeostasis, we further conducted an investigation comparing the individual and combined effects of BPTES and PGA on non-senescent MSCs. As shown in Supplementary Fig. 5A, the significantly lowest cell viability in the BPTES group indicated the inhibited proliferation of non-senescent MSCs (Supplementary Fig. 2C, no significant cytotoxicity). Meanwhile, BPTES also significantly reduced the concentrations of key metabolites in glutamine metabolism, including glutamate and α -KG, within non-senescent MSCs (Supplementary Fig. 5B). It is noteworthy that PGA not only rescued the proliferation of non-senescent MSCs but also significantly restored their glutamine metabolism. Additionally, ALP staining and quantitative analysis results demonstrated that PGA significantly rescued the inhibition of osteogenic differentiation of non-senescent MSCs caused by BPTES (Supplementary Fig. 5C).

The above results confirmed that the combination of BPTES and PGA could effectively achieve specific elimination of senescent cells while preserving the osteogenic differentiation potential of non-senescent MSCs, which provides a potential strategy for achieving effective implant osteointegration in elderly patients.

Construction and characterization of modified titanium implants

Based on the above theoretical basis, we developed a modified titanium implant incorporating a metabolic intervention strategy for orthopedic applications in elderly patients. The sample preparation process is outlined in Fig. 1. The samples were denoted as Ti, MT, MT-NH₂, BPTES@MNT, and BPTES@MNT/PGA. The physicochemical properties of the samples were characterized. As shown in Fig. 2A, environmental scanning electron microscopy (ESEM) was used to characterize the surface topography of each sample. Compared to Ti, the MT, BPTES@MNT, and BPTES@MNT/PGA showed a typical rigid microstructure. Compared to MT, BPTES@MNT displayed a typical micro-nano composite structure due to dopamine assembly, indicating dopamine nanoparticle formation on the implant substrate. The self-assembly of multilayers resulted in a visible coating over the

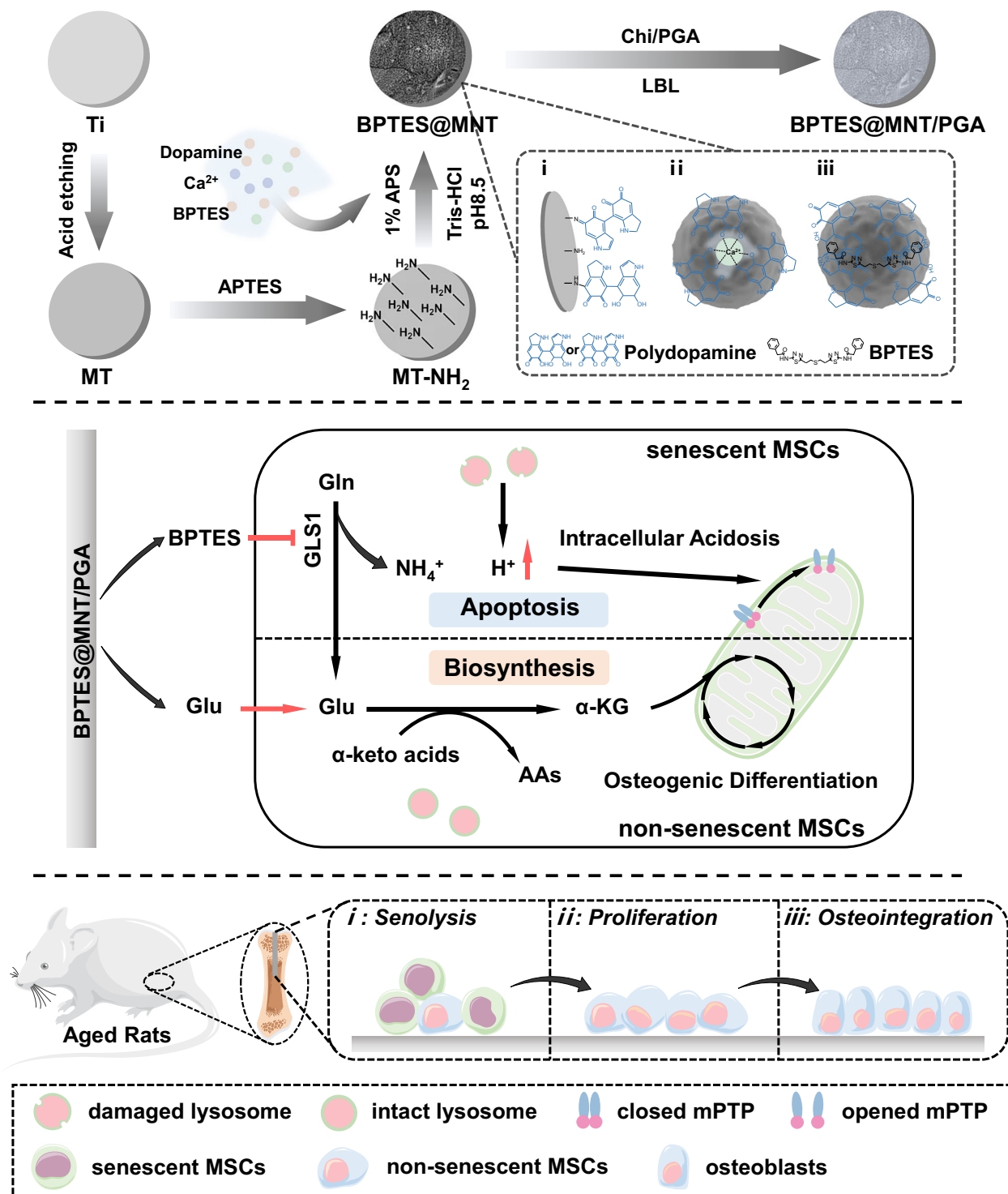


Fig. 1 | Design strategy for implant surface with engineered metabolic modulation. Schematic illustration of the design and preparation of the modified titanium implants. The modified implants specifically induce apoptosis in senescent MSCs by restricting glutaminolysis while rescuing glutamine metabolism in non-senescent MSCs by supplementing glutamate without ammonia production.

The topological structure of the implant surface and enhanced glutamine metabolism synergistically promote MSC osteogenic differentiation, thereby accelerating implant osteointegration in aged rats. Parts of the figure were drawn using pictures from Servier Medical Art. Servier Medical Art by Servier is licensed under a Creative Commons Attribution 4.0 International License.

micro-nano structure of BPTES@MNT/PGA. Correspondingly, the sample roughness measurement aligned with the observed morphology (Fig. 2B). Following acid etching treatment and the formation of a micro-nano composite structure, the surface roughness of the samples increased gradually. Subsequently, the roughness decreased with the multilayer coating, indicating successful PGA coating. Hydrophilicity was assessed using the water contact angle. As shown in Fig. 2C, the

average water contact angle of Ti was approximately 51.2°, significantly higher than that of MT (around 12.7°). Although MT-NH₂ did not exhibit significant differences in topology or roughness compared to MT, its average water contact angle was significantly higher (about 49.5°) due to the hydrophobicity of the silane coupling agent (Supplementary Fig. 6A). The micro-nano composite structure reduced the average water contact angle to approximately 39.1°, which

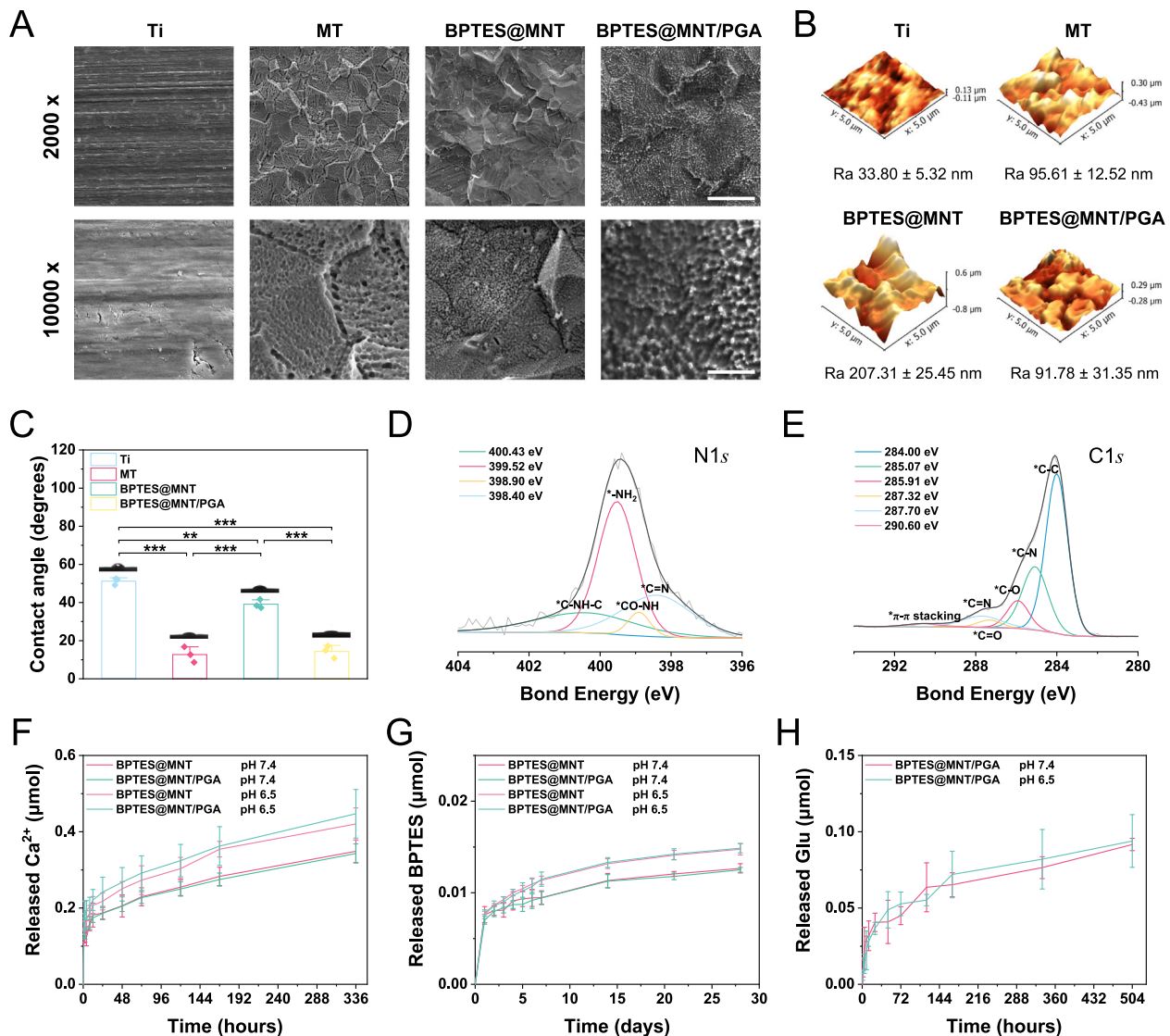


Fig. 2 | Characterization of BPTES@MNT/PGA and the release kinetics at implant interfaces. **A** Representative ESEM images of different samples. 2000 \times : Scale bar = 40 μm ; 10,000 \times : Scale bar = 8 μm . **B** AFM images of different samples. Surface Ra roughness data of different samples is shown at the bottom of the image ($n = 3$ independent samples per group). **C** The water contact angle of different samples ($n = 3$ independent samples per group). High-resolution XPS spectra of **D** N1s scan and **E** C1s scan of BPTES@MNT/PGA. Release profile of **F** Ca^{2+} , **G** BPTES,

and **H** Glu at different pH values ($n = 3$ independent samples per group). Data was presented as means \pm SD ($*p < 0.05$, $**p < 0.01$, $***p < 0.001$). Data analysis was conducted utilizing one-way ANOVA with Tukey's multiple comparison test (**C**). Data analysis was conducted by using a two-tailed unpaired Student t test (**F-H**). Exact P values were given in the Source data file. Source data are provided as a Source data file.

was due to the increased specific surface area and polydopamine hydrophilicity. The multilayer construction further increased hydrophilicity, with the average water contact angle of BPTES@MNT/PGA being about 14.3 $^\circ$.

X-ray Photoelectron Spectroscopy (XPS) was employed to analyze the elemental composition of the samples. BPTES@MNT exhibited characteristic peaks for Ca and S, confirming the successful incorporation of calcium ions and BPTES (Supplementary Fig. 6B). Analysis of the XPS spectra for N1s and C1s of BPTES@MNT revealed $*\text{C-NH-C}$ and $*\text{C=N}$ signals, indicating a Michael reaction between polydopamine and the titanium substrate, and $*\pi-\pi$ -stack signals, indicating the interaction between BPTES and polydopamine. (Fig. 2D, E). The encapsulation efficiency of BPTES was approximately 81.84%, and the coating density of about 16.37 $\mu\text{g}/\text{cm}^2$. X-ray diffractometry (XRD) patterns showed that the polydopamine coating existed in an amorphous state on the implant substrate (Supplementary Fig. 6C), suggesting effective Ca^{2+} release³⁵.

Release kinetics at the implant interface

Considering the physiological condition of a slightly acidic pH level in the orthopedic injury microenvironment³⁶, we investigated the release kinetics of implants at different pH environments. The release curves for Ca^{2+} revealed no significant difference between BPTES@MNT and BPTES@MNT/PGA, indicating that the PGA coating did not affect Ca^{2+} release (Fig. 2F). However, a reduction in pH accelerated Ca^{2+} release to a degree, though not statistically significant compared to pH 7.4. BPTES release followed a similar trend (Fig. 2G), with a notable acceleration of release at pH 6.5 after 7 days, likely due to the acid-degradable properties of polydopamine³⁷.

Given that the PGA coating is designed to degrade into glutamate as an exogenous carbon source for cells, we also examined the release curves of glutamate for BPTES@MNT/PGA. As shown in Fig. 2H, the pH changes did not significantly affect PGA degradation, with glutamate release reaching approximately 0.065 $\mu\text{mol}/\text{cm}^2$ (pH 7.4) and 0.072 $\mu\text{mol}/\text{cm}^2$ (pH 6.5) over 7 days. The release did not plateau after

21 days of incubation, indicating that PGA serves as a high-density carbon source coating, providing a rapid and sustained glutamate supply at the implant-host interface.

Cytocompatibility evaluation

To ensure the application of implants in orthopedic treatment settings, we conducted a cytocompatibility evaluation. Non-senescent ECs, non-senescent osteoblasts, and non-senescent MSCs were all evaluated to ensure the applicability of the implant. As shown in live/dead staining, no significant cytotoxicity was observed in any group across all cell types (Supplementary Fig. 7B, D, F). Notably, after 24 h of incubation, the CCK-8 assay results revealed that the cell viability of all cell types in the BPTES@MNT group was significantly lower than that in the Ti and MT groups (Supplementary Fig. 7A, C, E), indicating that BPTES@MNT severely inhibited the proliferation of all cell types, which might be associated with the inhibition of glutaminolysis. BPTES@MNT/PGA partially restored the cell viability of all cell types, which might be attributed to PGA-mediated rescue of glutamine metabolism.

BPTES@MNT/PGA specifically induced the apoptosis of senescent MSCs by affecting intracellular pH stability

Given the pivotal role of GLS1 in the survival of senescent MSCs, we hypothesized that BPTES@MNT/PGA could selectively induce apoptosis in these MSCs by inhibiting glutaminolysis. The mechanism of apoptosis induced by BPTES@MNT/PGA is shown in Fig. 3A. GLS1 activity was analyzed in both senescent and non-senescent MSCs after 1 day of incubation with various samples. As shown in Fig. 3B, GLS1 activities were significantly lower in the BPTES@MNT and BPTES@MNT/PGA groups compared to the Ti and MT groups, indicating effective inhibition of GLS1. Notably, in senescent MSCs, intracellular pH levels were significantly lower in the BPTES@MNT and BPTES@MNT/PGA groups compared to Ti and MT groups, consistent with prior studies and related to lysosomal leakage in senescent cells (Fig. 3C)^{25,38,39}. Correspondingly, BPTES@MNT and BPTES@MNT/PGA induced significant mPTP opening in senescent MSCs, indicative of apoptosis (Fig. 3D). However, no significant effect was observed in non-senescent MSCs (Supplementary Fig. 8). Flow cytometry and CCK-8 assays confirmed that BPTES@MNT and BPTES@MNT/PGA significantly induced apoptosis in senescent MSCs, with viability rates only about 66.33% and 58.15%, respectively (Fig. 3E). For non-senescent MSCs, MSCs showed no notable cytotoxicity, with viability rates above 80%. However, BPTES@MNT and BPTES@MNT/PGA groups exhibited reduced cell viability in non-senescent MSCs compared to other groups, indicating inhibited proliferation (Fig. 3F). Notably, after 3 days of incubation, non-senescent MSC viability on BPTES@MNT/PGA increased significantly, suggesting that PGA coating might rescue glutamine metabolism and promote their proliferation.

BPTES@MNT/PGA inhibited the secondary senescence induced by senescent MSCs

Senescent MSCs can exacerbate and propagate senescence through the SASP, potentially leading to implantation failure⁴⁰. Eliminating senescent cells could inhibit secondary senescence⁴¹. To verify this, the supernatant of senescent MSCs incubated with different samples was analyzed (Fig. 4A). As shown in Fig. 4B, compared to Ti and MT, BPTES@MNT and BPTES@MNT/PGA significantly reduced levels of various SASP factors, including IFN- γ , IL-1 β , IL-6, TNF- α , and peroxide, in the supernatant. Additionally, SA- β -gal staining revealed that BPTES@MNT and BPTES@MNT/PGA groups resulted in significantly lower SA- β -gal-positive regions in non-senescent MSCs compared to Ti and MT (Fig. 4C, E). BPTES@MNT and BPTES@MNT/PGA groups also exhibited stronger osteogenic differentiation potential than Ti and MT groups (Fig. 4D, F). These findings confirmed that BPTES@MNT/PGA could inhibit secondary senescence by selectively inducing apoptosis

in senescent MSCs, thereby preserving the osteogenic differentiation potential of non-senescent MSCs around the implant (Fig. 4G).

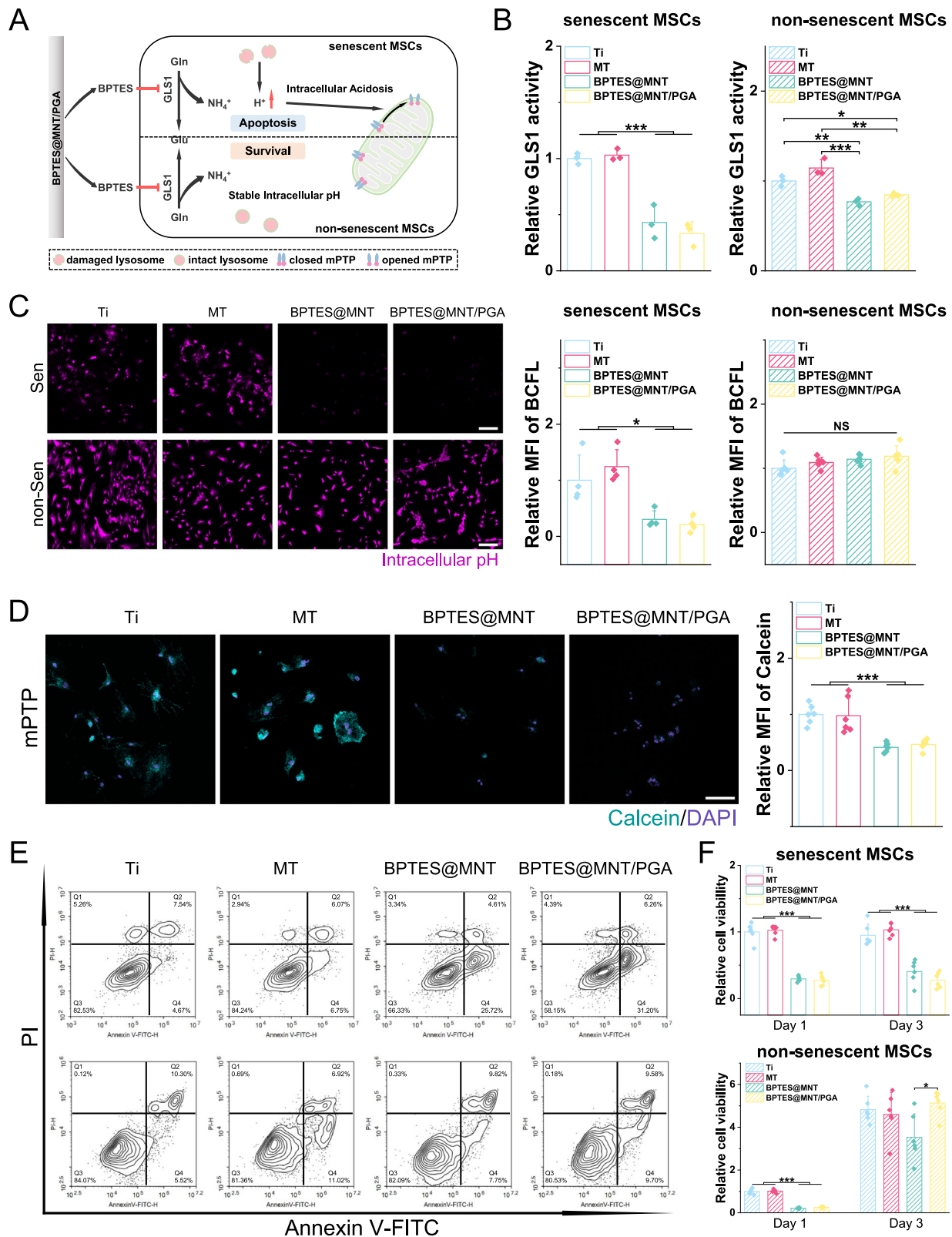
BPTES@MNT/PGA regulated the metabolic profile of non-senescent MSCs by rescuing glutamine metabolism

While inhibiting glutaminolysis specifically induced apoptosis in senescent MSCs, it also limited the proliferation of non-senescent MSCs (Fig. 3F). To determine whether PGA coating could rescue glutamine metabolism in non-senescent MSCs through glutamate supplementation, the glutamine metabolism levels in each group were analyzed. As shown in Fig. 5A, BPTES@MNT/PGA significantly increased the concentrations of downstream products of glutamine metabolism, such as glutamate, alanine, aspartate, and proline. Notably, intracellular glutamine levels in BPTES@MNT and BPTES@MNT/PGA groups were significantly higher than those in other groups, further indicating glutaminolysis inhibition, consistent with GLS1 activities results.

Targeted metabolic analysis revealed significant differences in the glycolysis pathway between BPTES@MNT and BPTES@MNT/PGA groups compared to Ti and MT. (Fig. 5B). BPTES@MNT and BPTES@MNT/PGA groups exhibited lower intracellular glucose, glucose-6-phosphate, and fructose-6-phosphate, suggesting increased glucose consumption. Notably, the BPTES@MNT/PGA group showed elevated intracellular pyruvate and active tricarboxylic acid cycle (TCA cycle), indicating enhanced aerobic glycolysis of MSCs. The BPTES@MNT group displayed the highest isocitrate/ α -KG ratio (Supplementary Fig. 9A), suggesting that the TCA cycle of MSCs was limited by a high ATP/ADP ratio. Intriguingly, the BPTES@MNT group had lower intracellular ATP compared to other groups (Supplementary Fig. 9B), with a significantly higher succinate/fumarate ratio (Supplementary Fig. 9C), indicating mitochondrial oxidative stress⁴² and elevated intracellular reactive oxygen species (ROS) levels (Supplementary Fig. 9D). The BPTES@MNT/PGA group had a significantly higher intracellular α -ketoglutarate (α -KG) than the BPTES@MNT, supporting the role of PGA in promoting glutamine metabolism. The higher intracellular gluconate in BPTES@MNT/PGA suggested an enhanced pentose phosphate pathway (PPP). BPTES@MNT/PGA group also showed the lowest intracellular ribose-5-phosphate but the highest intracellular adenosine monophosphate and guanosine monophosphate, indicating the active biosynthesis of MSCs. Additionally, BPTES@MNT/PGA group showed the highest intracellular amino acids (Supplementary Fig. 9E) (excluding cysteine) and higher intracellular L-carnitine compared to Ti and BPTES@MNT, suggesting active FAO of MSCs⁴³. These data indicated that BPTES@MNT/PGA positively regulated the metabolic profile of non-senescent MSCs and enhanced their biosynthesis by rescuing glutamine metabolism (Fig. 5C). The metabolic profile of MSCs in the BPTES@MNT/PGA group, characterized by enhanced aerobic glycolysis, PPP, glutamine metabolism, and FAO, along with higher intracellular hydroxyproline (a collagen-specific amino acid), suggests a strong potential for promoting the osteogenic differentiation of non-senescent MSCs^{27,44}.

BPTES@MNT/PGA promoted the osteogenic differentiation of non-senescent MSCs in vitro

The role of BPTES@MNT/PGA in promoting osteogenic differentiation of non-senescent MSCs was further verified. To account for the potential influence of Ca²⁺ released from samples on osteogenic differentiation, we analyzed the intracellular Ca²⁺ level of MSCs incubated with different samples (Supplementary Fig. 10). Notably, the MT, BPTES@MNT, and BPTES@MNT/PGA groups showed significantly higher intracellular Ca²⁺ levels compared to the Ti group, with increases of approximately 1.74, 1.66, and 1.65 times, respectively. However, no significant differences were observed among the MT, BPTES@MNT, and BPTES@MNT/PGA groups. These results suggest



that the Ca^{2+} released from implants does not primarily drive the osteogenic differentiation of non-senescent MSCs.

Subsequently, a Western blot was conducted to evaluate the osteogenic differentiation of non-senescent MSCs after incubation with different samples (Fig. 6A–D). The BPTES@MNT/PGA group exhibited significantly higher levels of collagen type I (Col I), alkaline phosphatase (ALP), and osteocalcin (OCN) compared to the Ti group,

indicating that BPTES@MNT/PGA possesses a stronger ability to promote osteogenic differentiation. Meanwhile, the BPTES@MNT group also demonstrated significantly higher levels of Col I than the Ti group, aligning with the intracellular hydroxyproline levels. Furthermore, the MT group also showed a certain degree of osteogenic differentiation-promoting effect (significantly higher levels of Col I and ALP than the Ti group), which might be due to its topological structure^{40,45}. Similar

Fig. 3 | BPTES@MNT/PGA specifically induced apoptosis in senescent MSCs. **A** Schematic illustration of the apoptosis in senescent MSCs specifically induced by BPTES@MNT/PGA. **B** Relative GLSI activity of senescent and non-senescent MSCs on different samples ($n = 3$ biologically independent samples per group). **C** Representative fluorescence images and quantification of intracellular pH in senescent ($n = 4$ biologically independent samples per group) and non-senescent ($n = 6$ biologically independent samples per group) MSCs on different samples. Scale bar = 200 μm . **D** Representative fluorescence images and quantification of mPTP in senescent MSCs on different samples ($n = 6$ biologically independent samples per group). Scale bar = 100 μm . **E** Apoptosis analysis of senescent and

non-senescent MSCs on different samples. **F** Cell viability of senescent and non-senescent MSCs after incubated with different samples for 1 and 3 days ($n = 6$ biologically independent samples per group). Data were presented as means \pm SD ($*p < 0.05$, $**p < 0.01$, $***p < 0.001$, NS no significant difference). Data analysis was conducted utilizing one-way ANOVA with Tukey's multiple comparison test. Exact P values were given in the Source data file. Source data are provided as a Source data file. Parts of the figure were drawn by using pictures from Servier Medical Art. Servier Medical Art by Servier is licensed under a Creative Commons Attribution 4.0 International License.

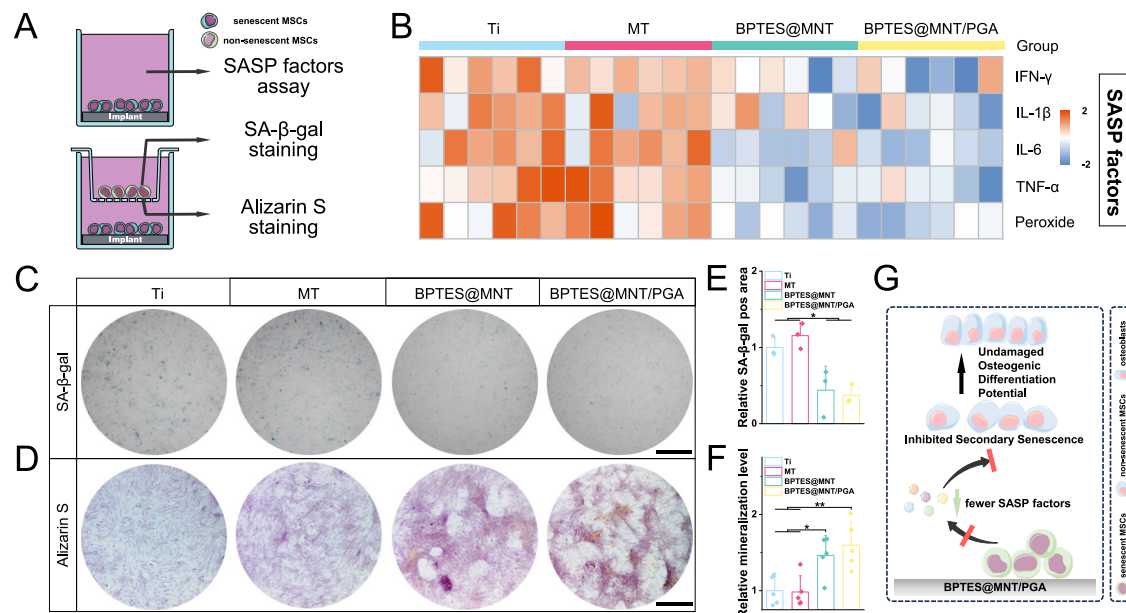


Fig. 4 | BPTES@MNT/PGA inhibited the secondary senescence induced by senescent MSCs. **A** Schematic illustration of SASP factors analysis and co-culture setup. **B** Heatmap for SASP factors (IFN- γ , IL-1 β , IL-6, TNF- α , and Peroxide) analysis. **C** Representative images and **E** quantitative statistics of SA- β -gal in each group after incubation for 3 days ($n = 3$ biologically independent samples per group). Scale bar = 1 mm. **D** Representative images and **F** quantification of alizarin red staining in each group after incubation for 14 days ($n = 5$ biologically independent samples per

group). Scale bar = 500 μm . **G** Schematic illustration of inhibited secondary senescence mediated by BPTES@MNT/PGA. Data were presented as means \pm SD ($*p < 0.05$, $**p < 0.01$). Data analysis was conducted utilizing one-way ANOVA with Tukey's multiple comparison test. Exact P values were given in the Source data file. Source data are provided as a Source data file. Parts of the figure were drawn by using pictures from Servier Medical Art. Servier Medical Art by Servier is licensed under a Creative Commons Attribution 4.0 International License.

results were obtained in the mineralization analysis (Fig. 6E, F). Notably, although the BPTES@MNT group did not exhibit significantly higher expression levels of osteogenic-related proteins compared to the MT group, its mineralization level was significantly elevated. This phenomenon might be attributed to the enhanced mineralization promoted by the Ca^{2+} released from implants.

BPTES@MNT/PGA eliminated the senescent cells and promoted the proliferation of endogenous stem cells in vivo

The efficacy of BPTES@MNT/PGA was further verified in vivo using 18-month-old rats as a senescent model (Fig. 7A). We assessed the senescence level around the implant. As shown in Fig. 7B, the p16 expression level around the implant in the BPTES@MNT and BPTES@MNT/PGA groups was significantly lower than that in the Ti and MT groups. The p16/DAPI ratio around the implant in the BPTES@MNT/PGA group was only about 0.27 times that in the Ti group (Fig. 7D). The flow cytometry results showed that the BPTES@MNT/PGA group had the lowest proportion of SA- β -gal $^{+}$ cells (40.5%) in bone marrow (Supplementary Fig. 11), significantly lower than that in the Ti group (64.9%), confirming the effective elimination of senescent cells. Additionally, compared to the Ti and MT groups, significantly reduced inflammatory cell infiltration and markedly lower levels of inflammatory factors (IL-1 β and IL-6) were observed around the implant in the BPTES@MNT and

BPTES@MNT/PGA groups (Supplementary Fig. 12A and Supplementary Fig. 13), which was consistent with the decreased senescence level of tissue.

Given the potential proliferation-inhibiting effects of the modified implants observed in vitro (Fig. 3F)³², we further evaluated the proliferation level around the implant. The distribution of stem cells (leptin receptor-expressing (LepR $^{+}$)) was also assessed simultaneously (Fig. 7C)^{46,47}. The BPTES@MNT group exhibited the lowest proliferation activity and the fewest stem cells around the implant (Fig. 7E, F), consistent with the in vitro results. The LepR expression level (LepR/DAPI ratio) in the BPTES@MNT/PGA group was significantly increased by approximately 3.06 times compared to the BPTES@MNT group. Partial spatial colocalization with Ki67 was also observed, suggesting relatively active stem cell proliferation in the BPTES@MNT/PGA group. Hematoxylin and eosin (HE) and Masson staining further demonstrated the robust ability of BPTES@MNT/PGA to promote stem cell proliferation. The BPTES@MNT/PGA group exhibited a significantly higher number of osteoblasts and osteocytes around the implant compared to other groups, indicating active cell proliferation (Supplementary Fig. 12A). In addition, the BPTES@MNT/PGA group showed markedly thicker fibrous bone-like structures and pronounced bone formation around the implant compared to the other groups (Supplementary Fig. 12B).

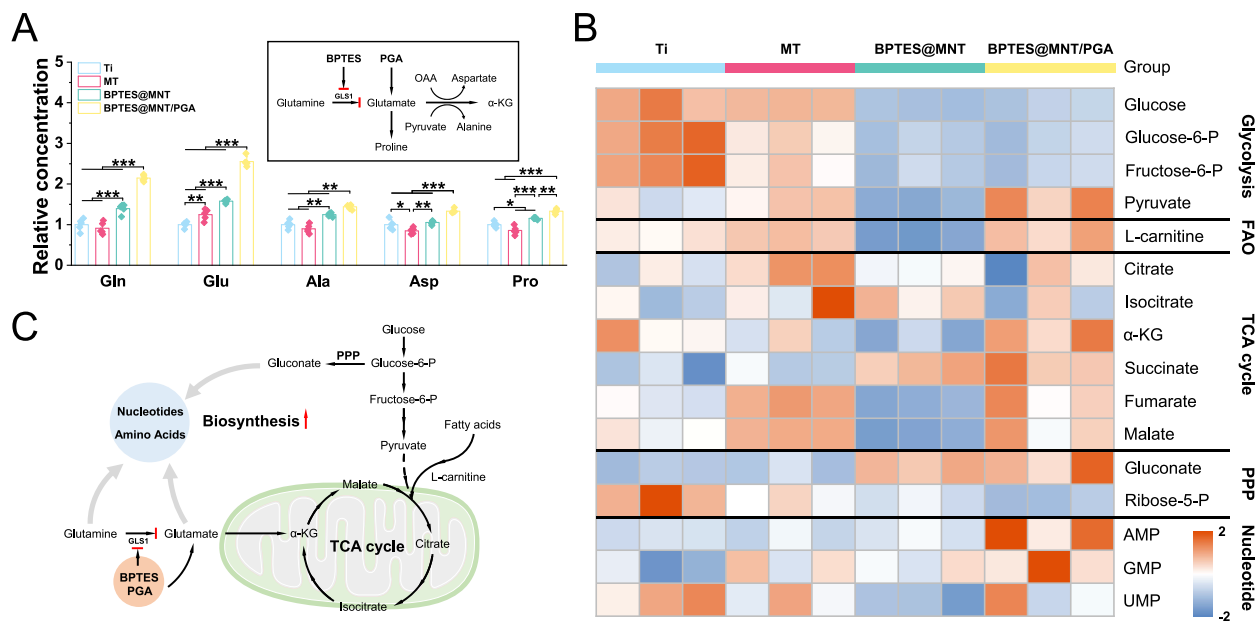


Fig. 5 | BPTES@MNT/PGA regulated the metabolic profile of non-senescent MSCs. **A** Effectiveness of different samples on the metabolite concentration of glutamine metabolism ($n = 5$ biologically independent samples per group). The schematic of BPTES@MNT/PGA on rescuing glutamine metabolism is shown in the box. **B** Heatmap represented differentially detected metabolites in different groups associated with glycolysis, FAO, TCA cycle, PPP, and anabolic metabolism. **C** Schematic illustration of metabolic profile in non-senescent MSCs

regulated by BPTES@MNT/PGA. Data was presented as means \pm SD ($*p < 0.05$, $**p < 0.01$, $***p < 0.001$). Data analysis was conducted utilizing one-way ANOVA with Tukey's multiple comparison test. Exact P values were given in the Source data file. Source data are provided as a Source data file. Parts of the figure were drawn by using pictures from Servier Medical Art. Servier Medical Art by Servier is licensed under a Creative Commons Attribution 4.0 International License.

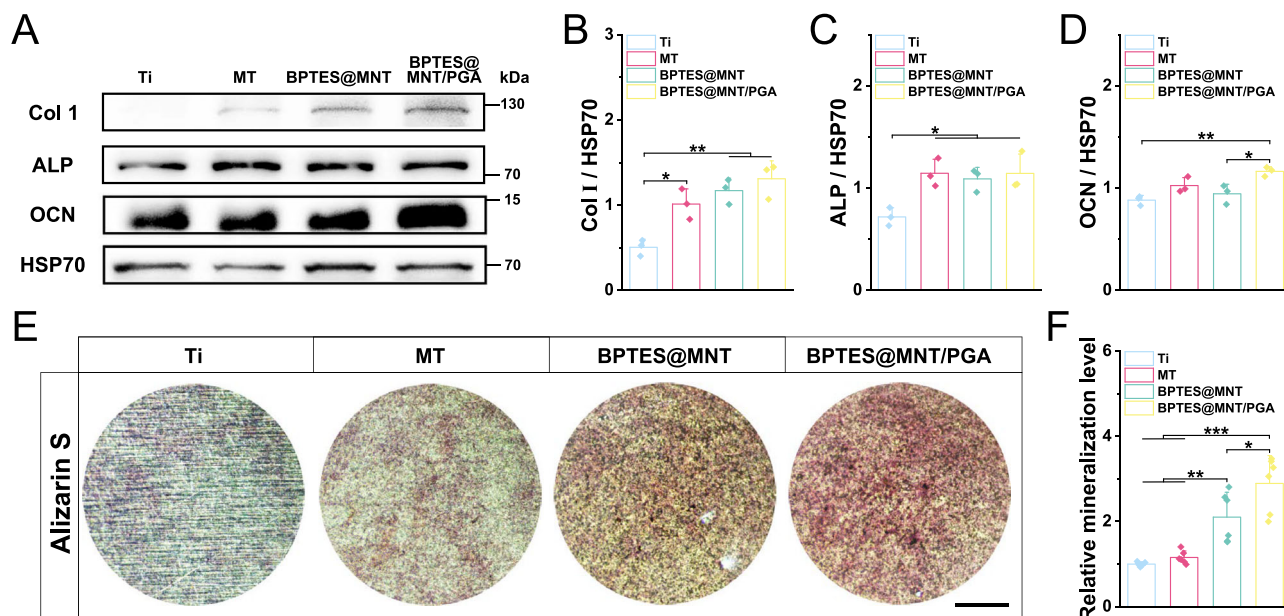


Fig. 6 | BPTES@MNT/PGA promoted the osteogenic differentiation of non-senescent MSCs. **A–D** Western blot results for Col I, ALP, and OCN in non-senescent MSCs after incubated with different groups for 7 days ($n = 3$ biologically independent samples per group). **E** Representative images and **F** quantification of alizarin red staining in each group after incubation for 14 days ($n = 6$ biologically

independent samples per group). Scale bar = 500 μ m. Data was presented as means \pm SD ($*p < 0.05$, $**p < 0.01$, $***p < 0.001$). Data analysis was conducted utilizing one-way ANOVA with Tukey's multiple comparison test. Exact P values were given in the Source data file. Source data are provided as a Source data file.

Enhanced osteointegration of BPTES@MNT/PGA implant in aged rats

After 6 weeks of implantation, μ -CT analysis was performed to evaluate the osteointegration of each implant. The BPTES@MNT/PGA group exhibited the highest bone mass (BV/TV) around the implant

compared to all groups (Fig. 8B–H). In addition, the BPTES@MNT/PGA group also showed most trabecular number (Tb.N), the thickest trabecular thickness (Tb.Th), and the lowest trabecular spacing (Tb.Sp) among all groups. Notably, the structure model index (SMI) indicated that the trabeculae structure around the implant in the BPTES@MNT/

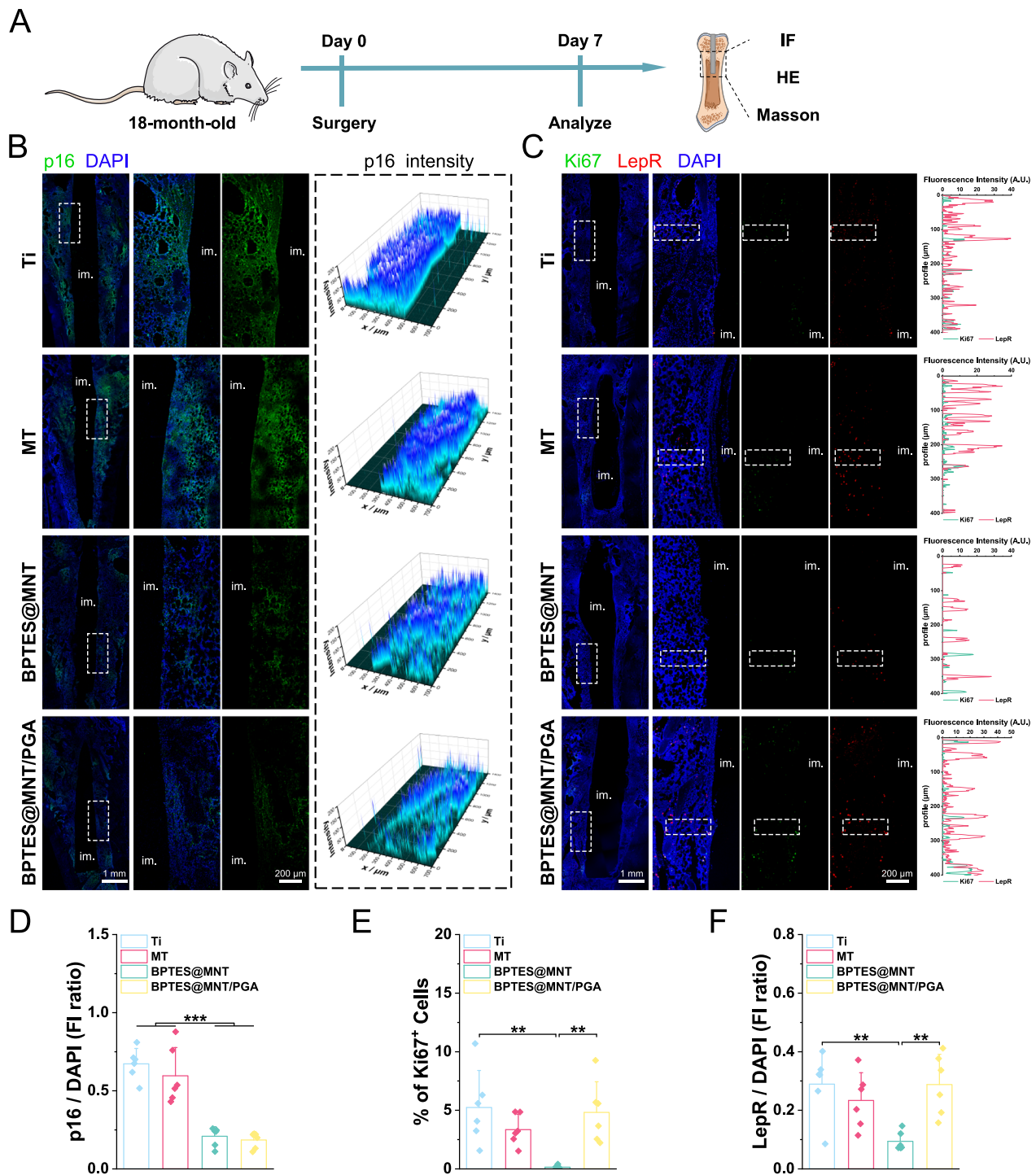


Fig. 7 | BPTES@MNT/PGA eliminated the senescent cells and promoted the proliferation of endogenous stem cells in vivo. **A** Schematic illustration of in vivo analysis. **B** Representative fluorescence images and corresponding 3D profiles (White box selection area) of the intensity of p16 around implants. **C** Representative fluorescence images and colocalization analysis (White box selection area) of Ki67 and LepR around implants. **D–F** Quantitative statistics of Ki67, TUNEL, p16, and

LepR around implants ($n = 6$ biologically independent samples per group). Key: im., implants. Data were presented as means \pm SD (** $p < 0.01$, *** $p < 0.001$). Exact P values were given in the Source data file. Source data are provided as a Source data file. Parts of the figure were drawn by using pictures from Servier Medical Art. Servier Medical Art by Servier is licensed under a Creative Commons Attribution 4.0 International License.

PGA group was predominantly plate-like, in contrast to a rod-like structure in other groups, suggesting enhanced stability of the implants in the BPTES@MNT/PGA group. Interestingly, the bone mineral density (BMD) around the implant in the BPTES@MNT/PGA group was significantly higher than that in the BPTES@MNT group, further emphasizing the importance of PGA coating in enhancing

implant osteointegration by rescuing glutamine metabolism. Mechanical push-out testing was further conducted to evaluate the integration of the implant with surrounding bone tissue (Fig. 8I). As shown in Fig. 8J, K, BPTES@MNT/PGA achieved the highest maximal push-out force (60.58 ± 8.26 N), which was significantly higher than that in the other groups. Meanwhile, the results of

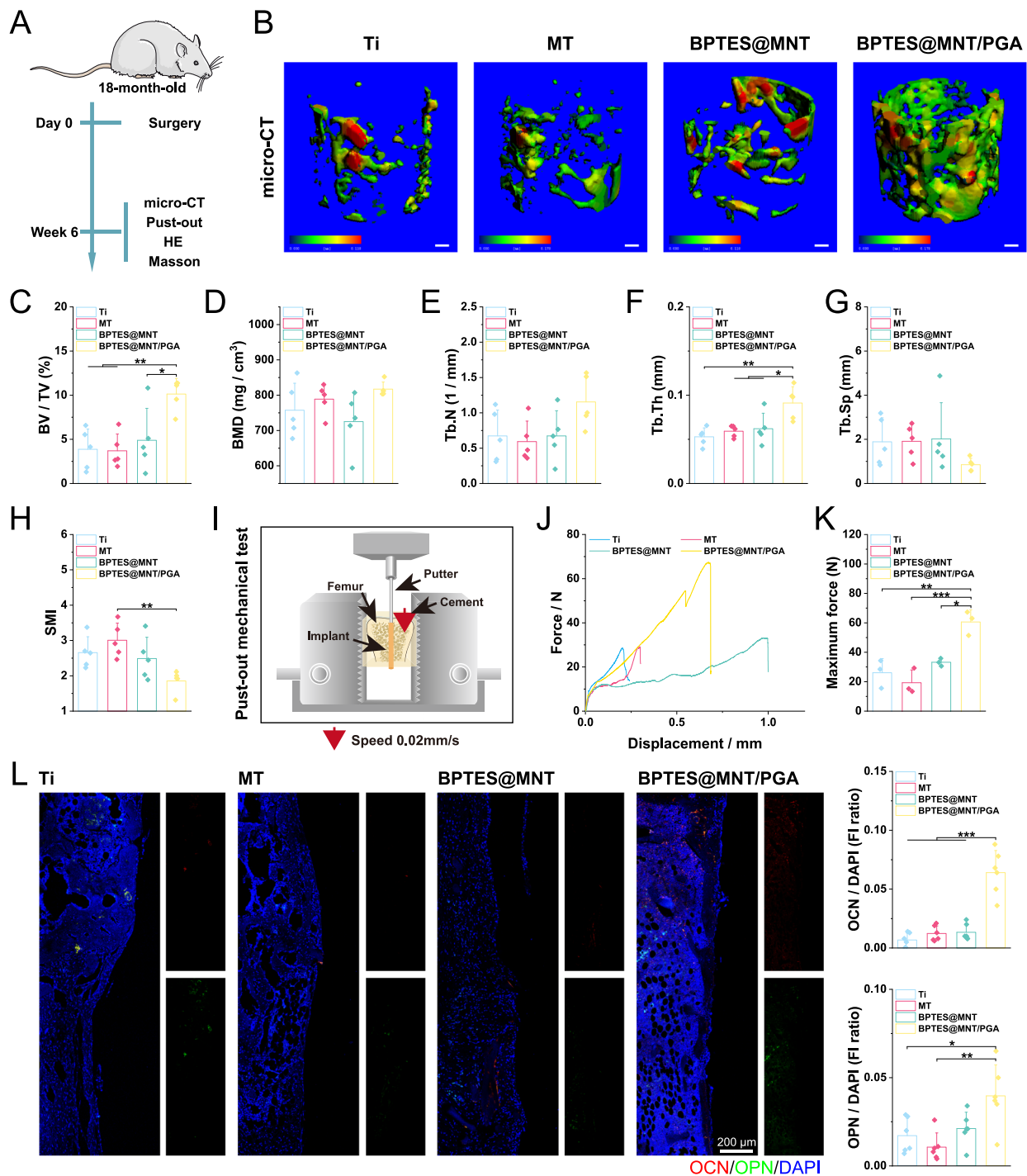


Fig. 8 | Enhanced osteointegration of BPTES@MNT/PGA implant in aged rats.

A Schematic illustration of in vivo analysis. **B** Three-dimensional μ -CT reconstructions around implants after 6 weeks of surgery. Scale bar = 200 μ m. **C–H** Analysis of μ -CT data showing BV/TV, SMI, BMD, Tb.N, Tb.Th and Tb.Sp around implants ($n = 5$ biologically independent samples per group). **I** Schematic illustration of bio-mechanical push-out testing. **J** Representative push-out testing curves of different groups. **K** Maximum push-out force in different groups ($n = 3$ biologically

independent samples per group). **L** Representative fluorescence images and quantitative staining analysis of OCN and OPN around implants. Data was presented as means \pm SD (* $p < 0.05$, ** $p < 0.01$, *** $p < 0.001$). Exact P values were given in the Source data file. Source data are provided as a Source data file. Parts of the figure were drawn by using pictures from Servier Medical Art. Servier Medical Art by Servier is licensed under a Creative Commons Attribution 4.0 International License.

immunofluorescence and Masson staining demonstrated that the BPTES@MNT/PGA group exhibited the significantly highest level of osteogenic-related protein expression (OCN and OPN) and the most mature and continuous bone (Fig. 8L and Supplementary Fig. 14). HE staining was used to evaluate the long-term biocompatibility of implants (Supplementary Fig. 14B). A small number of inflammatory

cell infiltrations could be observed around the implant in both the Ti and MT groups, which might be associated with long-term chronic inflammation caused by the higher senescence level⁴⁸. In contrast, the BPTES@MNT/PGA group showed no significant inflammatory cell infiltration around the implant, along with well-formed bone regeneration. Notably, the BPTES@MNT group showed significantly more

fibrotic structures around the implant, both in HE and Masson staining, suggesting the potential adverse effects of BPTES@MNT due to the sustained inhibition of glutamine metabolism. All data demonstrated that the BPTES@MNT/PGA implants achieved more stable osteointegration in aged rats than other implants.

Discussion

In this study, a modified titanium implant was developed to target senescent cells specifically and enhance the osteointegration in aged rats. The modified implant features a micro-nano composite structure, created through in-situ polymerization of dopamine nanoparticles on a ridge structure after acid etching. Ca^{2+} and $-\text{NH}_2$ served as binding sites, allowing for the smooth loading of BPTES. This micro-nano structure is believed to facilitate osteogenic differentiation of MSCs⁴⁰ and provides an increased specific surface area that benefits the application of polymer coatings⁴⁹.

The non-covalent binding of the modified implant allowed for effective release of both BPTES and PGA. BPTES was used to inhibit glutaminolysis, thereby inducing apoptosis in senescent cells. PGA was degraded into glutamate, which was then taken up by MSCs to effectively rescue glutamine metabolism. Notably, the amount of BPTES released from modified titanium within 3 days (approximately $0.01\ \mu\text{mol}$) was insufficient to inhibit the proliferation of non-senescent MSCs in vitro (Supplementary Fig. 2B). However, BPTES@MNT still exhibited a significantly inhibitory effect on the proliferation of non-senescent MSCs (Fig. 3F), likely due to the improved delivery efficiency of BPTES through direct diffusion from the coating to cells⁵⁰. This diffusion mode also ensured the clearance of senescent cells around the implant, which was verified both in vivo and in vitro. Meanwhile, the presence of PGA coating directed rescued (without ammonia production) the inhibited glutamine metabolism, which enabled BPTES@MNT/PGA could specifically induce apoptosis of senescent MSCs while maintaining the proliferation ability of non-senescent MSCs.

The specific elimination of senescent cells by BPTES was attributed to its restriction on free ammonia production, which was associated with the dependence of senescent cells on free ammonia generation caused by lysosomal leakage^{22,25}. In contrast, non-senescent cells maintain relatively stable intracellular pH levels, as they do not experience lysosomal leakage issues triggered by macromolecular damage. Additionally, PGA rescued the BPTES-mediated inhibition of glutamine metabolism in non-senescent MSCs by supplementing glutamate. The carbon skeleton of glutamate contributed to anabolism through the TCA cycle as $\alpha\text{-KG}$, and its amino group supported the synthesis of amino acids via aminotransferase. Meanwhile, the amino group of glutamine could also be involved in the de novo synthesis of purine and pyrimidine nucleotides, counteracting the effects of glutaminolysis. Intriguingly, BPTES@MNT/PGA increased the concentration of most amino acids in non-senescent MSCs, except for cysteine. This reduction in cysteine may be attributed to its increased consumption for glutathione production, one of the main products of glutamine metabolism, consistent with the lowest intracellular ROS levels observed in the BPTES@MNT/PGA group.

Ca^{2+} released from implants did not affect intracellular Ca^{2+} levels, a result likely due to both the limited concentration of released Ca^{2+} and the regulatory mechanism of intracellular Ca^{2+} ⁵¹. The increase in intracellular Ca^{2+} , driven by the topological structure, was associated with the osteogenic differentiation of non-senescent MSCs. However, the osteogenic differentiation of non-senescent MSCs in the MT group was still limited by its lower anabolic activity (high ATP/ADP ratio (isocitrate/ $\alpha\text{-KG}$ ratio)), highlighting the need for an additional carbon source. In addition, extracellular Ca^{2+} released from the modified implants contributed to the mineralization process, providing BPTES@MNT capacity to promote osteogenic differentiation in vitro. Despite the successful elimination of senescent cells, BPTES@MNT

showed poor osteointegration in vivo, which was consistent with in vitro results (lowest cell proliferation, lowest ATP production, and highest intracellular ROS level). Notably, after 6 weeks, severe fibrotic tissue formation appeared around BPTES@MNT implants, further emphasizing the importance of rescuing glutamine metabolism for long-term osteointegration of implants.

Different from our previous reported modified titanium implant (MNT-PDA/GelHA) engineered through a SASP factors secretion suppression and proliferation activation way⁵², BPTES@MNT/PGA enhanced osteointegration in aged rats via coordinated senolytic and osteogenic differentiation, effectively mitigating age-related constraints on the application of implants. Benefiting from the elimination of senescent cells, BPTES@MNT/PGA not only promoted osteointegration in advanced-aged rats (18 months old) but also circumvented the potential chronic impairments to implant stability induced by senescence cells.

However, compared with the mild osteointegration strategy of MNT-PDA/GelHA, the potential side effects of the more aggressive senolytic therapy may pose significant challenges for the clinical application of BPTES@MNT/PGA in the future. This necessitates further systematic and comprehensive in vivo investigations into the underlying mechanisms of BPTES@MNT/PGA. In vivo gain/loss functional analyses may serve as an effective approach to further elucidate the mechanism of BPTES@MNT/PGA in the future, further validating the efficacy of the directed rescue strategy and providing theoretical foundations for the clinical application of BPTES@MNT/PGA.

In summary, BPTES@MNT/PGA was constructed based on a directed rescue strategy to specifically eliminate senescent cells and enhance osteogenic differentiation of non-senescent MSCs, thereby improving osteointegration in aged rats (Fig. 1). BPTES@MNT/PGA effectively disrupted the intracellular pH homeostasis of senescent MSCs while meeting the high anabolic demands of non-senescent MSCs through glutamate supplementation. This reduction in secondary senescence and enhanced osteogenic differentiation synergistically promoted the osteointegration of BPTES@MNT/PGA in aged rats, providing valuable insights for the design of orthopedic implants for elderly patients.

Methods

Ethical statement

The animal experiments were approved by the Animal Ethics Committees of the Chongqing Medical University (2021-738) and carried out in strict accordance with the guidelines and relevant laws. All animals were provided by Chongqing Medical University (SCXK 2022-0010).

Materials

Titanium foils and rods were purchased from Alfa Aesar Co. (Tianjin, China). Chitosan (Chi), calcium chloride anhydrous (CaCl_2), dopamine hydrochloride, tris base, ammonium persulfate (APS), (3-aminopropyl)-triethoxysilane (APTES), poly(γ -glutamate) (PGA), and cobalt (II) chloride (CoCl_2) were purchased from Aladdin Industrial Co. (Shanghai, China). BPTES were purchased from MedChemExpress LLC. (NJ, USA). Cell counting kit-8 (CCK-8) was purchased from APEX BIO Technology LLC. (TX, USA). RatioWorks™ BCFL AM was purchased from ATT Bioquest Inc. (CA, USA). DAPI, Triton X-100, alizarin red sodium, glutamate content assay kit (WST colorimetry), and micro glutaminase (GLS) assay kit were bought from Solarbio Science & Technology Co., Ltd. (Beijing, China). Senescence-associated β -galactosidase (SA- β -gal) staining kit, ROS assay kit, calcein AM, RIPA lysis buffer, bovine serum albumin (BSA), etoposide, calcium assay kit, Annexin V-FITC apoptosis detection kit, and Fluo-4 AM were purchased from Beyotime Biotechnology Co. (Jiangsu, China). Rat IFN- γ , IL-1 β , IL-6, and TNF- α ELISA kits were purchased from Shanghai Enzyme-linked Biotechnology Co., Ltd. (Shanghai, China). Anti-p21,

Anti-p16, Anti-OCN, and Anti-ALP were purchased from ABclonal Inc. (Hubei, China). Anti-GLS1, Anti-KGA, Anti-Ki67, Anti-LepR, Anti-Col 1, Anti-HSP27, Anti-VDAC1, and Anti-GAPDH were purchased from Proteintech Group, Inc. (Hubei, China). Anti-OPN was purchased from Affinity Biosciences (OH, USA). Anti-BNIP3 was purchased from Abcam (Cambridge, UK). Anti-HSP-70 was purchased from Beijing Biosynthesis Biotechnology Co., Ltd. (Beijing, China). Other chemicals were provided by Oriental Chemical Co. (Chongqing, China).

Cell isolation and culture

MSCs were isolated from Sprague-Dawley rats (male, 4-week-old) with the differential adhesion method. The obtained MSCs were donated as non-senescent MSCs and cultured in DMEM medium (low glucose, supplemented with 10% fetal bovine serum and 1% penicillin/streptomycin) and then incubated at 37 °C under 5% CO₂ atmosphere. Cells at passage three were used for *in vitro* experiments. MC3T3-E1 (Subclone 14, with the catalog number of CRL-2594) and Human Umbilical Vein Endothelial Cells (HUVECs, CP-H082) were purchased from Wuhan Pricella Biotechnology Co., Ltd. MSCs were authenticated (Supplementary Fig. 15) by the rat mesenchymal stem cell identification kit (Cyagen); MC3T3-E1 cell lines were authenticated by the supplier using Short Tandem Repeat (STR). HUVECs were authenticated by the supplier using IF staining of CD31.

For replicative senescent MSCs, MSCs were passaged nine times to lose their proliferation ability. For induced-senescent MSCs, MSCs were treated with 20 mM etoposide for 12–18 h and then cultured in fresh medium for 3 days to ensure that they lost the capacity for proliferation. The cellular senescence was evaluated by SA- β -gal staining and immunofluorescence staining of p16 and p21 (senescence markers), and non-senescent MSCs were selected as the control.

Western blot

RIPA lysis buffer (containing PMSF (100:1, Beyotime)) was used to extract the total protein of MSCs. The total proteins were separated by SDS-polyacrylamide gels (Bio-Rad) and then blotted onto the 0.45 μ m polyvinylidene fluoride membrane. After blocking with 5% BSA solution for 60 min, the membrane was incubated with primary antibody (1:1000) at 4 °C overnight, and then incubated with horseradish peroxidase-conjugated secondary antibody (1:5000, Beyotime) for another 60 min. A multifunctional imaging system (SCG-W5000, Servicebio) was used to detect the signal. The intensity of bands was normalized to the internal control protein.

Cell viability

The cell viability of MSCs in different samples was detected by the CCK-8 assay. After 3 and 7 days of incubation, the medium of each group was discarded, and CCK-8 solution (10%) was added to each well. After incubating for 2 h, the supernatant of each sample was analyzed by a spectrophotometric microplate reader (Bio-Rad 680).

Assessment of apoptosis

The apoptosis levels were detected by Annexin V-FITC apoptosis detection kit (Beyotime) according to the manufacturer's instructions. Analytical Flow Cytometry (Novocyt Advantec, Agilent, USA) was used to detect the signal. The data was analyzed by NovoExpress software.

Cell fractionation and alkaline treatment

Cell mitochondria isolation kit (Beyotime) was used to separate mitochondria and cytosolic proteins. After being thoroughly lysed with mitochondrial isolation reagent and homogenized with a Dounce homogenizer, the samples were split into two. The pH of one-half was adjusted to 11.0 with 0.1 M Na₂CO₃ and incubated on ice for 20 min. Subsequently, cytoplasmic fractions and mitochondrial fractions were separated and collected according to the manufacturer's instructions.

α -KG content analysis

The α -KG content was determined by the Amplex Red α -KG Assay Kit (Beyotime). Experimental procedures were performed strictly following the manufacturer's protocol. Fluorescence measurements were conducted using a multifunctional microplate reader. Normalization of protein quantification was performed by the BCA Protein Assay Kit (Beyotime) to eliminate differences in cell count between samples.

Surface modification of titanium

MT was constructed by acid etching. Briefly, the titanium was sequentially treated with 3 wt% hydrofluoric acid at room temperature for 2 min and then immersed in 66 wt% sulfuric acid at 80 °C for 5 min. The obtained MT was rinsed thoroughly with ultrasonics. Subsequently, MT was immersed in 3% APTES solution (toluene as solvent) for 24 h, and then washed thoroughly for further use.

BPTES@MNT was obtained by one-step polymerization of dopamine. Briefly, MT-NH₂ was placed in a mixed solution ($V_{\text{Tris-HCl buffer (10 mM, pH 8.5)}}: V_{\text{DMSO}} = 1:1$) containing dopamine (1 mg/mL), CaCl₂ (0.05 mg/mL), BPTES (0.05 mg/mL), and 1% APS. The reaction mixture was under continuous shaking (40 rpm) at room temperature overnight and avoid light. The obtained samples were rinsed thoroughly with DI water.

Subsequently, PGA coating was modified on the substrate of BPTES@MNT by the layer-by-layer method. In short, the samples were alternately immersed in Chi (0.5 w/v%) and PGA (1 w/v%) solution (two repeats). The samples were sterilized with ultraviolet irradiation or prepared under an aseptic environment for subsequent *in vitro* and *in vivo* experiments.

Characterization of samples

The topographic and hydrophilic characteristic of each sample was characterized by ESEM (Quattro S, Thermo Fisher Scientific, USA), atomic force microscopy (AFM, Dimension, Bruker, Germany), and a video-based optical system (Model 200, Future Scientific Co., Taiwan, China). The interfacial bonding mechanism of BPTES@MNT/PGA was identified by XPS (ESCALAB 250Xi, Thermo Fisher Scientific, USA). The surface crystalline phase of the samples was detected by XRD (Empyrean, Panalytical B.V., Holland).

Released profiling of Ca²⁺, BPTES, and glutamate

For Ca²⁺ and glutamate analysis, samples were immersed in PBS (pH 7.4 or pH 6.5) under continuous shaking (40 rpm) at 37 °C. After being incubated for a specific time, the supernatant was harvested, and the fresh PBS was replenished. The Ca²⁺ and glutamate content in each supernatant sample were measured by the calcium assay kit and glutamate content assay kit, respectively.

For BPTES analysis, samples were immersed in DMSO/PBS (1:1, v/v, pH 7.4 or pH 6.5) under continuous shaking (40 rpm) at 37 °C. The supernatant was harvested at predetermined intervals, and the fresh PBS was replenished each time. The BPTES content in each supernatant sample was measured by a liquid chromatography mass spectrometry (LC-MS/MS, LCMS-8060, SHIMADZU Corporation, Japan).

GLS1 activity analysis

GLS1 activity of cell lysates was determined using a micro glutaminase (GLS) assay kit (Solarbio) according to the manufacturer's instructions. Cells incubated with different samples for 1 day were collected to analyze.

Intracellular pH analysis

Intracellular pH of each group was evaluated by BCFL AM. After incubated with different samples, the medium of each group was discarded, and BCFL AM working solution (10 μ M) was added into each well. After incubation for 30 min, the samples were washed thoroughly

with PBS and then observed by a confocal laser scanning microscopy (CLSM, TCS SP8, Leica, GER).

Mitochondrial permeability transition pore (mPTP) analysis

Briefly, Calcein AM was used to assess the changes in mPTP. After washing thoroughly with PBS, the serum-free medium (containing 0.1 μ M Calcein AM and 0.4 mM CoCl_2) was added into each well for 30 min at 37 °C. Then, fresh medium was replaced and incubated for another 30 min to ensure adequate hydrolysis of Calcein AM. Washed with PBS for three times, the samples were observed by CLSM.

Enzyme-linked immunosorbent assay (ELISA)

Medium of each sample was collected after 3 days of incubation and then centrifuged for 20 min at 500 g. Then the supernatant was collected, and the secretion of interferon- γ (IFN- γ), interleukin-1 β (IL-1 β), interleukin-6 (IL-6), and tumor necrosis factor α (TNF- α) was detected.

Medium peroxide detection

Hydrogen peroxide assay kit (Beyotime) was used according to the manufacturer's instructions. After 3 days of incubation with different groups, the medium was collected, and the contained peroxide was measured.

Intracellular ROS detection

Intracellular ROS levels were detected by a ROS assay kit (Beyotime). Briefly, 0.1% v/v of DCFH-DA was added to incubate the samples for 20 min. After rinsing thoroughly, the cells were then imaged by CLSM.

Targeted metabolic analysis

Targeted metabolites were analyzed using liquid chromatography-electrospray ionization-tandem mass spectrometry (LC-ESI-MS/MS). Data preprocessing and annotation were performed by Majorbio BioPharm Technology.

Central carbon metabolites analysis was performed using the ExionLC AD system (SCIEX) with a UPLC HSS T3 column (1.8 μ m, 2.1 \times 150 mm; Waters Corporation) coupled to the QTRAP 6500+ (SCIEX). Briefly, 0.5×10^7 cells were combined with 10 μ L of internal standard solution (containing 5 μ g/mL succinate-D4, 5 μ g/mL L-carnitine-D3, 20 μ g/mL cholic acid-D4, and 30 μ g/mL salicylic acid-D4), 50 μ L of methanol solution (methanol: water = 1:1, fisher) and 140 μ L of acetonitrile. Then the mixed solution was vortexed for 1 min and sonicated for 30 min at 4 °C. After sonication, the sample was centrifuged at 14,000 \times g for 20 min at 4 °C, and 100 μ L of supernatant was collected. 25 μ L of 3-NPH HCL (200 mM) and 25 μ L of EDC HCL (120 mM, containing 6% pyridine) were added, and then the mixed solution was vortexed for 30 s and placed into a constant temperature oscillator for 40 min at 60 °C. Finally, the sample was centrifuged at 14,000 \times g for 20 min at 4 °C, and the supernatant was collected for analysis. Chromatographic separation was set at 40 °C, with a mobile phase comprising water containing 0.03% formic acid (solvent A) and methanol containing 0.03% formic acid (solvent B). Mass spectrometry analysis was set in both positive and negative modes. The temperature was set to 550 °C, curtain gas was maintained at 35 psi, collision gas was set to medium, and both ion source gases 1 and 2 were set to 55 psi. Ion-spray voltage was set to 4500 V/–4500 V.

For amino acids analysis, 0.5×10^7 cells were combined with 4 μ L of internal standard solution (containing 100 μ g/mL L-Trp-D5, L-Gln-D5, and L-Lys-D4), 216 μ L purified water (Fisher), and 25 μ L of 0.15% DOC. The mixed solution was sonicated for 10 min at 5 °C, and then 5 μ L of trichloroacetic acid (10 M) was added. Before centrifugation, the sample was stored at –20 °C for 10 min. Then the sample was centrifuged at 14,000 \times g for 10 min at 4 °C, and 50 μ L of supernatant was collected. Three hundred fifty microliters of purified water were added, and then the mixed solution was filtered by a PTFE filter (0.2 μ m, biotage) for further analysis. Chromatographic separation

was achieved using an AdvanceBio MS Spent Media (2.7 μ m, 2.1 \times 50 mm) set to 40 °C, with a mobile phase comprising water containing 0.1% formic acid and 10 mM ammonium formate (solvent A), and acetonitrile containing 0.1% formic acid and 10 mM ammonium formate (solvent B). QTRAP 6500+ (SCIEX) was used to analyze, and the system was set in both positive and negative modes. The temperature was set to 550 °C, curtain gas was maintained at 35 psi, collision gas was set to medium, and both ion source gases 1 and 2 were set to 50 psi. Ion-spray voltage was set to 5500 V/–4500 V.

The LC-MS raw data were analyzed by Sciex software OS, with ion fragments automatically identified and integrated using default parameters. Manual inspection was performed to confirm the quality of the data, and the metabolite concentrations of the samples were determined by comparing the peak areas of the analytes with those of the internal standards, using a linear regression standard curve.

Intracellular Ca²⁺ detection

Fluo-4 AM was used to detect the intracellular Ca²⁺ of non-senescent MSCs. After washed thoroughly with PBS, 0.5 μ M Fluo-4 AM (PBS as solvent) was added into each well for 30 min at 37 °C. Then, fresh PBS was replaced and incubated for another 20 min to ensure adequate hydrolysis of Fluo-4 AM. Washed with PBS for three times, the samples were observed by CLSM.

Mineralization analysis

After cultured for 14 days, cells were stained with alizarin red sodium solution (0.1%, pH 4.1). The image data were collected by a stereomicroscope (MVX10, Olympus, Japan). After dissolving the stained mineral nodules in a 10% v/v acetic acid solution and then mixing with a 10% ammonia solution, a spectrophotometric microplate reader (Bio-Rad 680) was used to collect the quantitative data.

Animal and bone defect model construction

Sprague-Dawley rats (male, 18 months old) were randomly allocated into four groups: (1) Ti; (2) MNT; (3) MNT-PDA, and (4) MNT-PDA/GelHA ($n = 15$ for each group), and 2% pentobarbital was administered for preoperative anesthesia. The surgical site was disinfected with iodophor. The femoral bone defect was created by a surgical drill on the patellar femoral surface. The sterilized titanium rod was then slowly implanted into the defect site. All surgical procedures were performed under an aseptic environment. Female exclusion was implemented to control for estrogen influences on osteoporosis.

Immunofluorescence staining of bone tissue sections

The obtained tissue samples were fixed overnight, and then decalcified in a 0.5M EDTA solution (pH 7.4) under constant oscillation at 4 °C. After paraffin embedding, the samples were sectioned into 10- μ m-thick sections. 1% citrate antigen retrieval solution was used for the antigenic repair of sections (95 °C, 10 min), and 5% BSA solution was used for the blocking of sections (37 °C, 10 min). The primary antibody (anti-p16, anti-Ki67, anti-LepR, anti-IL-6, anti-IL-1 β , anti-OCN, anti-OPN) was added to adequately cover the sections and incubated overnight. After TBS-T cleaning, the secondary antibody (Alexa Fluor 488-labeled antibody or Alexa Fluor 647-labeled antibody, Beyotime) was then added to incubate the samples for another 30 min. Finally, DAPI was used to stain the nucleus. Glycerin was used to seal the sections to prevent fluorescence quenching. The sections were imaged by CLSM, and the data were analyzed by ImageJ.

In vivo flow cytometry analysis

CellEvent™ Senescence Green Flow Cytometry Assay Kit (Thermo Fisher Scientific) was used to detect the senescence level in vivo. Seven days after the implantation surgery, the femurs were harvested, and bone marrow cells were isolated. Nucleated cells were separated using Red Blood Cell Lysis Buffer (Beyotime). The cells were processed

strictly following the manufacturer's protocol. Analytical Flow Cytometry (Beckman Coulter CytoFLEX LX) was used to detect the signal. The data was analyzed by FlowJo.

Histological staining analysis

The sections were also stained by the HE and Masson methods. The HE stain kit (Solarbio) and Masson's trichrome stain kit (Solarbio) were used according to the manufacturer's instructions. The sections were imaged by a Digital Slicing Workstation (Olympus, VS120), and the data were analyzed by OlyVIA and ImageJ.

μ -CT analysis

The osteointegration of the implant was analyzed by μ CT100 (Scanco Medical, CH) with a setting of 70 kV, 200 μ A (resolution of 14.8 μ m/pixel). The parameters and 3D models of osteointegration around the implants were obtained by the SCANCO Medical microCT system.

Biomechanical push-out testing

The biomechanical push-out testing was performed using an in-situ mechanical test system (CARE Measurement & Control, China). Before the tests, the samples were fixed vertically to the base using dental cement. The implant was pushed out with a displacement rate of 1.2 mm/min. The test was stopped when the screw was completely separated from the bone. The maximum push-out force was recorded to evaluate the mechanical stability. Each group had three parallel replicates.

Data availability

Targeted metabolomics raw data have been deposited in Metabolomics Workbench with the Project ID: PR002634 (Project <https://doi.org/10.21228/M85V83>). All other data generated in this study are provided in the Supplementary Information/Source data file. Source data are provided with this paper.

References

- He, S. & Sharpless, N. E. Senescence in health and disease. *Cell* **169**, 1000–1011 (2017).
- Ambrosi, T. H. et al. Aged skeletal stem cells generate an inflammatory degenerative niche. *Nature* **597**, 256–262 (2021).
- Moiseeva, V. et al. Senescence atlas reveals an aged-like inflamed niche that blunts muscle regeneration. *Nature* **613**, 169–178 (2022).
- Farr, J. N. et al. Targeting cellular senescence prevents age-related bone loss in mice. *Nat. Med.* **23**, 1072–1079 (2017).
- Qu, A. et al. An NIR-responsive DNA-mediated nanotetrahedron enhances the clearance of senescent cells. *Adv. Mater.* **32**, 2000184 (2020).
- Cai, Y. et al. Elimination of senescent cells by β -galactosidase-targeted prodrug attenuates inflammation and restores physical function in aged mice. *Cell Res.* **30**, 574–589 (2020).
- Kim, S. et al. Supramolecular senolytics via intracellular oligomerization of peptides in response to elevated reactive oxygen species levels in aging cells. *J. Am. Chem. Soc.* **145**, 21991–22008 (2023).
- Power, H., Valtchev, P., Dehghani, F. & Schindeler, A. Strategies for senolytic drug discovery. *Aging Cell* **22**, e13948 (2023).
- Dolgin, E. Send in the senolytics. *Nat. Biotechnol.* **38**, 1371–1377 (2020).
- Gorgoulis, V. et al. Cellular senescence: defining a path forward. *Cell* **179**, 813–827 (2019).
- Childs, B. G., Durik, M., Baker, D. J. & van Deursen, J. M. Cellular senescence in aging and age-related disease: from mechanisms to therapy. *Nat. Med.* **21**, 1424–1435 (2015).
- Yuan, L., Alexander, P. B. & Wang, X. F. Cellular senescence: from anti-cancer weapon to anti-aging target. *Sci. China Life Sci.* **63**, 332–342 (2020).
- Crespo-Garcia, S. et al. Pathological angiogenesis in retinopathy engages cellular senescence and is amenable to therapeutic elimination via BCL-xL inhibition. *Cell Metab.* **33**, 818–832 (2021).
- Xu, Q. et al. The flavonoid procyanidin C1 has senotherapeutic activity and increases lifespan in mice. *Nat. Metab.* **3**, 1706–1726 (2021).
- Wilson, W. H. et al. Navitoclax, a targeted high-affinity inhibitor of BCL-2, in lymphoid malignancies: a phase 1 dose-escalation study of safety, pharmacokinetics, pharmacodynamics, and antitumour activity. *Lancet Oncol.* **11**, 1149–1159 (2010).
- Justice, J. N. et al. Senolytics in idiopathic pulmonary fibrosis: results from a first-in-human, open-label, pilot study. *EBioMedicine* **40**, 554–563 (2019).
- Victorelli, S. et al. Apoptotic stress causes mtDNA release during senescence and drives the SASP. *Nature* **622**, 627–636 (2023).
- Glück, S. et al. Innate immune sensing of cytosolic chromatin fragments through cGAS promotes senescence. *Nat. Cell Biol.* **19**, 1061–1070 (2017).
- Molinari, M. ER-phagy responses in yeast, plants, and mammalian cells and their crosstalk with UPR and ERAD. *Dev. Cell* **56**, 949–966 (2021).
- Newman, L. E. et al. Mitochondrial DNA replication stress triggers a pro-inflammatory endosomal pathway of nucleoid disposal. *Nat. Cell Biol.* **26**, 194–206 (2024).
- Castro, J. P. et al. Non-enzymatic cleavage of Hsp90 by oxidative stress leads to actin aggregate formation: a novel gain-of-function mechanism. *Redox Biol.* **21**, 101108 (2019).
- Skowyra, M. L., Schlesinger, P. H., Naismith, T. V. & Hanson, P. I. Triggered recruitment of ESCRT machinery promotes endolysosomal repair. *Science* **360**, eaar5078 (2018).
- Hao, T. et al. Hypoxia-reprogramed megamitochondrion contacts and engulfs lysosome to mediate mitochondrial self-digestion. *Nat. Commun.* **14**, 4105 (2023).
- Wong, Y. C., Ysselstein, D. & Krainc, D. Mitochondria-lysosome contacts regulate mitochondrial fission via RAB7 GTP hydrolysis. *Nature* **554**, 382–386 (2018).
- Johmura, Y. et al. Senolysis by glutaminolysis inhibition ameliorates various age-associated disorders. *Science* **371**, 265–270 (2021).
- McHugh, D. et al. COPI vesicle formation and N-myristoylation are targetable vulnerabilities of senescent cells. *Nat. Cell Biol.* **25**, 1804–1820 (2023).
- van Gestel, N. & Carmeliet, G. Metabolic regulation of skeletal cell fate and function in physiology and disease. *Nat. Metab.* **3**, 11–20 (2021).
- Chen, M. et al. ROS-activatable biomimetic interface mediates in-situ bioenergetic remodeling of osteogenic cells for osteoporotic bone repair. *Biomaterials* **291**, 121878 (2022).
- van Gestel, N. et al. Lipid availability determines fate of skeletal progenitor cells via SOX9. *Nature* **579**, 111–117 (2020).
- Karner, C. M., Esen, E., Okunade, A. L., Patterson, B. W. & Long, F. Increased glutamine catabolism mediates bone anabolism in response to WNT signaling. *J. Clin. Investig.* **125**, 551–562 (2015).
- Stegen, S. et al. Glutamine metabolism in osteoprogenitors is required for bone mass accrual and PTH-induced bone anabolism in male mice. *J. Bone Min. Res.* **36**, 604–616 (2021).
- Yu, Y. et al. Glutamine metabolism regulates proliferation and lineage allocation in skeletal stem cells. *Cell Metab.* **29**, 966–978 (2019).
- Kubasiak, L. A., Hernandez, O. M., Bishopric, N. H. & Webster, K. A. Hypoxia and acidosis activate cardiac myocyte death through the Bcl-2 family protein BNIP3. *Proc. Natl. Acad. Sci. USA* **99**, 12825–12830 (2002).
- Vande Velde, C. et al. BNIP3 and genetic control of necrosis-like cell death through the mitochondrial permeability transition pore. *Mol. Cell Biol.* **20**, 5454–5468 (2000).
- Zhu, S. et al. Microenvironment responsive nanocomposite hydrogel with NIR photothermal therapy, vascularization and anti-

- inflammation for diabetic infected wound healing. *Bioact. Mater.* **26**, 306–320 (2023).
36. Hazehara-Kunitomo, Y. et al. Acidic pre-conditioning enhances the stem cell phenotype of human bone marrow stem/progenitor cells. *Int J. Mol. Sci.* **20**, 1097 (2019).
 37. Yan, J. et al. Rapidly inhibiting the inflammatory cytokine storms and restoring cellular homeostasis to alleviate sepsis by blocking pyroptosis and mitochondrial apoptosis pathways. *Adv. Sci.* **10**, 2207448 (2023).
 38. Curnock, R. et al. TFEB-dependent lysosome biogenesis is required for senescence. *EMBO J.* **42**, e111241 (2023).
 39. Tan, J. X. & Finkel, T. Lysosomes in senescence and aging. *EMBO Rep.* **24**, e57265 (2023).
 40. Li, X. et al. Micronano titanium accelerates mesenchymal stem cells aging through the activation of senescence-associated secretory phenotype. *ACS Nano* **17**, 22885–22900 (2023).
 41. Zhao, R. et al. Precise diabetic wound therapy: PLS nanospheres eliminate senescent cells via DPP4 targeting and PARP1 activation. *Adv. Sci.* **9**, e2104128 (2022).
 42. Murphy, M. P. & O'Neill, L. A. J. Krebs cycle reimaged: The emerging roles of succinate and itaconate as signal transducers. *Cell* **174**, 780–784 (2018).
 43. Mller, D. M., Seim, H., Kiess, W., Lster, H. & Richter, T. Effects of oral L-carnitine supplementation on in vivo long-chain fatty acid oxidation in healthy adults. *Metabolism* **51**, 1389–1391 (2002).
 44. Udenfriend, S. Formation of hydroxyproline in collagen. *Science* **152**, 1335–1340 (1966).
 45. Zhao, L., Liu, L., Wu, Z., Zhang, Y. & Chu, P. K. Effects of micropitted/nanotubular titania topographies on bone mesenchymal stem cell osteogenic differentiation. *Biomaterials* **33**, 2629–2641 (2012).
 46. Jeffery, E. C., Mann, T. L. A., Pool, J. A., Zhao, Z. & Morrison, S. J. Bone marrow and periosteal skeletal stem/progenitor cells make distinct contributions to bone maintenance and repair. *Cell Stem Cell* **29**, 1547–1561 (2022).
 47. Zhou Bo, O., Yue, R., Murphy Malea, M., Peyer, J. G. & Morrison Sean, J. Leptin-receptor-expressing mesenchymal stromal cells represent the main source of bone formed by adult bone marrow. *Cell Stem Cell* **15**, 154–168 (2014).
 48. Josephson, A. M. et al. Age-related inflammation triggers skeletal stem/progenitor cell dysfunction. *Proc. Natl. Acad. Sci. USA* **116**, 6995–7004 (2019).
 49. Li, X. et al. ROS-responsive hydrogel coating modified titanium promotes vascularization and osteointegration of bone defects by orchestrating immunomodulation. *Biomaterials* **287**, 121683 (2022).
 50. Chen, Y. et al. Hydrophobic coating platforms for high-efficiency loading and direct transmembrane delivery of fat-soluble osteogenic drug for enhanced osseointegration of titanium implants. *Adv. Funct. Mater.* **34**, 2314005 (2024).
 51. Bagur, R. & Hajnóczky, G. Intracellular Ca²⁺ sensing: Its role in calcium homeostasis and signaling. *Mol. Cell* **66**, 780–788 (2017).
 52. Li, X. et al. Enhanced osteointegration of implants in aged rats via a stem cell pool aging reversion strategy. *Biomaterials* **325**, 123604 (2026).

Acknowledgements

The Analytical and Testing Center of Chongqing University is greatly acknowledged for its help with the characterization of materials. This

work was financially supported by the National Natural Science Foundation of China (Nos. 52333011, 52021004, 21734002 and 32171327 to K.C.), State Key Project of Research and Development (2022YFB3804400 to K.C.), and the Natural Science Foundation of Chongqing (No. cstc2021jcyj-cxttX0002 to K.C.).

Author contributions

X.L., X.J., H.X., Q.H., K.X., K.L., B.T. and K.Z. contributed to the collection of experimental data. X.L., X.J., H.X. and J.W. analyzed the data. X.L., Y.H., P.L. and K.C. contributed to writing and revising the paper. X.L., X-X.L. and K.X. contributed to formal analysis. K.C. supervised the research.

Competing interests

X.L., P.L. and K.C. have submitted a patent application to the China National Intellectual Property Administration pertaining to the surface modification technology of titanium and its applications aspects of this work (number CN202411313824.4, filed 20 September 2024). The other authors declare no competing interests.

Additional information

Supplementary information The online version contains supplementary material available at <https://doi.org/10.1038/s41467-025-65284-z>.

Correspondence and requests for materials should be addressed to Kaiyong Cai.

Peer review information *Nature Communications* thanks Hala Zreiqat and the other, anonymous, reviewer(s) for their contribution to the peer review of this work. A peer review file is available.

Reprints and permissions information is available at <http://www.nature.com/reprints>

Publisher's note Springer Nature remains neutral with regard to jurisdictional claims in published maps and institutional affiliations.

Open Access This article is licensed under a Creative Commons Attribution-NonCommercial-NoDerivatives 4.0 International License, which permits any non-commercial use, sharing, distribution and reproduction in any medium or format, as long as you give appropriate credit to the original author(s) and the source, provide a link to the Creative Commons licence, and indicate if you modified the licensed material. You do not have permission under this licence to share adapted material derived from this article or parts of it. The images or other third party material in this article are included in the article's Creative Commons licence, unless indicated otherwise in a credit line to the material. If material is not included in the article's Creative Commons licence and your intended use is not permitted by statutory regulation or exceeds the permitted use, you will need to obtain permission directly from the copyright holder. To view a copy of this licence, visit <http://creativecommons.org/licenses/by-nc-nd/4.0/>.

© The Author(s) 2025, modified publication 2026